Dual-band Modified Trapezoidal Antenna for Wireless Local Area Network (WLAN) and X-Band Communications

Suthasinee Lamultree [1,*], Punyawat Wiyanat [1], Kanit Butdaengnoi [1], and Chuwong Phongcharoenpanich [2]
[1] Department of Electronics and Telecommunication Engineering, Faculty of Engineering, Rajamangala University of Technology Isan Khonkaen Campus, Khonkaen, Thailand
[2] Department of Telecommunications Engineering, School of Engineering, King Mongkut's Institute of Technology, Ladkrabang, Bangkok, Thailand
Email: suthasinee.la@rmuti.ac.th (S.L.); punyawat1809@gmail.com (P.W.), NMKNTMN7905@gmail.com (K.B.); chuwong.ph@kmitl.ac.th (C.P.)

Manuscript received April 1, 2026; revised May 22, 2026; accepted June 1, 2026
*Corresponding author

***Abstract*—This research introduces a planar trapezoidal-shaped antenna for dual-band wireless communications. An inverted L-Shaped Strip (ILSS) is incorporated into the radiating structure with a 50-Ohm Coplanar Waveguide (CPW) feed on a single-layer FR4 substrate to generate dual resonant modes within a footprint (70 mm × 70 mm). The proposed design achieves impedance bandwidths of 1.86 GHz to 3.57 GHz and 7.12 GHz to 8.97 GHz ($|S_{11}| \leq -10$ dB), covering the 2.4 GHz WLAN band and the X-Band for Fixed-Satellite Service (FSS) applications. The dual-band behavior is attributed to the coupling between the modified trapezoidal patch and the ILSS, which introduces an additional current path and enhances impedance matching across both bands. It exhibits maximum gains of 2.72 dBi for the lower band and 3.8 dBi for the higher band, along with radiation efficiencies of up to 94.35% and 71.13%. Antenna performance was optimized using the electromagnetic microwave simulation tool Computer Simulation Technology (CST) and subsequently validated through the fabrication and measurement of a prototype, with good agreement and minor discrepancies between simulated and measured results. These findings confirm the antenna's suitability for Wireless Local Area Network (WLAN) 2.4 GHz applications and uplink/downlink X-band 7.825 GHz FSS applications. Furthermore, the 7.1 GHz to 8.4 GHz range emerges as a promising candidate for future wireless technologies, particularly 6G, due to its inherent capacity for high data rates, increased capacity, and advanced antenna implementations.**

***Index Terms*—dual-band antenna, fixed-satellite service, modified-trapezoidal patch, omnidirectional antenna, patch antenna, Wireless Local Area Network (WLAN) 2.4 GHz**

I. INTRODUCTION

Recent advances in wireless communication systems have significantly increased the demand for antennas capable of supporting multiple services across widely separated frequency bands. As networks migrate from traditional sub-GHz and lower-microwave allocations toward the upper-microwave and pre-THz spectral regions, there is increased demand for antennas capable of seamless operation across multiple, widely separated frequency bands [1−4]. These multi-band designs must simultaneously satisfy stringent size constraints, ease of fabrication, and stable radiation performance [3−5]. Capable multi-band operation facilitates seamless handover across diverse services, enhances spectrum utilization through carrier aggregation, and provides essential future-proofing against shifting standards. In dynamic wireless environments, such as mobile, wearable, Internet of Things (IoT), and Internet of Vehicles (IoV) ecosystems, maintaining omnidirectional radiation patterns is critical for ensuring reliable connectivity independent of device orientation [6−9]. To address these requirements, several geometrical and material-based techniques have been explored to excite multiple resonant modes within compact footprints.

A wide range of antenna configurations has been investigated to achieve compact dual-band and multiband operation for modern wireless applications. Among these approaches, metallic and hybrid wire-based radiators have demonstrated effective bandwidth enhancement. For example, Saeed *et al.* [8] employed a metallic wire-dicone structure combined with printed meander-line dipoles and stubs to achieve wide multiband coverage with high radiation efficiency; however, the resulting design exhibits increased structural complexity and limited suitability for planar integration. In contrast, Ashong *et al.* [9] proposed a multilayer microstrip patch antenna incorporating shorting vias, a coupled ring, and an embedded parasitic patch to realize dual-band operation, albeit with increased fabrication complexity due to its multilayer configuration. Transparent antennas based on Indium–Tin–Oxide (ITO) materials have also been reported to support visually unobtrusive integration; however, these designs generally suffer from reduced gain and radiation efficiency, particularly at higher frequencies [10].

For compact planar implementations targeting Wireless Local Area Network (WLAN) and related applications, various techniques have been explored to excite multiple resonant modes within limited footprints. Li *et al*. [11] introduced a miniaturized antenna using a ground-radiation technique, where coupling elements and ground-plane modifications were utilized to achieve dual-band operation at 2.4 GHz and 5 GHz to 7 GHz. Beyond conventional WLAN bands, increasing attention has been directed toward upper-microwave frequencies as candidates for next-generation wireless systems. The 7 GHz to 8.4 GHz spectrum has recently attracted attention as a potential candidate for future wireless systems, due to its balance between propagation capability and bandwidth availability [12]. At the same time, compact antenna solutions capable of supporting both microwave and X-band operations have been explored to enable multifunctional wireless platforms [13]. In addition, resonant perturbation methods, such as the incorporation of split-shaped circular rings, have been employed to transform ultra-wideband antennas into multiband radiators [14]. Modified trapezoidal geometries combined with tapered feed structures and partial ground planes have also been demonstrated as effective solutions for bandwidth enhancement while maintaining a compact planar profile [15].

More recent studies have focused on improving compactness and frequency selectivity through advanced loading techniques. Parasitic elements and Defected Ground Structures (DGS) have been widely used to achieve dual-band operation in compact and wearable antennas [16−18]. Similarly, slot-loading techniques applied to Planar Inverted-F Antennas (PIFAs) enable independent control of multiple resonant bands within constrained geometries [19]. Meanwhile, metamaterial-inspired and fractal-based designs have been proposed to realize multi-band or multifunctional performance; however, such approaches often introduce increased design complexity and reduced fabrication tolerance [20].

At the system level, dual-band antennas operating across widely separated frequency bands have gained increasing attention. For instance, duplex balun-based configurations have been introduced to enhance impedance matching and band isolation in base-station applications, although at the expense of structural complexity [21]. In addition, Multiple Input Multiple Output (MIMO)-based fractal antennas with modified ground structures have been developed to improve channel capacity in sub-6 GHz systems, but are not primarily optimized for compact dual-band operation [22].

With the growing interest in upper microwave and X-band frequencies for satellite communication, automotive radar, and emerging wireless systems, several designs have extended antenna operation into the 7 GHz to 8 GHz range. These antennas typically employ combinations of resonators, slots, stubs, or Artificial Magnetic Conductors (AMCs) to enhance gain and bandwidth [6, 23]. Hybrid radiator configurations, such as split-ring resonators and inverted-L-shaped loading elements, have also been investigated to excite multiple resonant modes within compact planar structures [24, 25]. Despite these advances, many of the reported designs rely on multilayer structures or intricate geometries, which may limit their suitability for compact, low-cost wireless integration.

Despite the substantial progress reported in the literature, achieving a low-profile, single-layer dual-band antenna that simultaneously offers wide impedance bandwidth, stable omnidirectional radiation patterns, and practical gain across both WLAN and X-band frequencies remains a challenging task. Many existing solutions rely on multilayer configurations, complex resonator arrangements, or specialized materials, which increase fabrication complexity and cost. Others suffer from limited upper-band bandwidth, reduced radiation efficiency, or degraded radiation stability at higher frequencies. Consequently, there is a clear research gap for a structurally simple planar antenna capable of supporting widely separated dual-band operation with balanced radiation performance, normalized electrical size, and suitability for low-cost wireless integration. Motivated by the challenges, this work proposes a compact dual-band antenna based on a modified trapezoidal-shaped radiator integrated with planar feeding structure. The antenna is designed to support WLAN and X-band communications within a single, low-profile configuration while preserving fabrication simplicity. The key contributions of this work can be summarized as follows:

- A planar antenna geometry employing a modified trapezoidal-shaped radiator that enables dual-band operation without the need for multilayer structures or complex resonant loading.
- Wide impedance bandwidth coverage for both WLAN and X-band frequency ranges, with particular emphasis on achieving enhanced bandwidth in the upper band.
- Stable omnidirectional radiation characteristics with practical gain and acceptable radiation efficiency across both operating bands.
- Design insight and parametric analysis that clarify the physical mechanisms responsible for dual-band resonance generation, facilitating reproducibility and future extensions of the proposed approach.

These features collectively position the proposed antenna as a practical and scalable solution for integrated WLAN and X-band wireless communication systems.

II. Procedure Specifically Designed

A. Design Layout and Equivalent Circuit

The layout of the dual-band patch antenna is shown in Fig. 1. The main radiating element is a Modified Trapezoidal Patch (MTP). This patch has an upper width (w_{p1}), a lower width (w_{p2}), and a length (l_p). It features a corner cut at a flare angle (α) on its lower edge to improve impedance matching. An Inverted-L Shape Strip (ILSS) is attached to the right side of the MTP at the height h_s above the lower edge of the MTP to increase the antenna's gain as well as impedance matching. The ILSS has a horizontal length (s_1), a vertical length (s_2), and a width (s_3). All these elements are made from a thick layer of copper. The antenna is fed by a 50-Ω Coplanar Waveguide (CPW) with a width (w_g) and a length (l_g), a 0.4 mm feed-to-ground gap (g_1), a feed-line length (l_f) of 17 mm, and a width (w_f) of 3 mm. The entire structure is built on a single-layer FR4 circuit board with a relative permittivity of 4.3 and a thickness (h) of 1.6 mm. The board dimensions are 70 mm × 70 mm. The separation between the patch and the ground plane, g_2, is 1.5 mm. The antenna is designed and optimized using Computer Simulation Technology (CST) Microwave Studio [26]. Through an iterative parameter adjustment process, the design was refined to meet key performance criteria, including a reflection coefficient $|S_{11}| \leq -10$ dB for good impedance matching and omni-directional radiation with gain greater than 2.5 dBi. The final optimized design parameters are provided in Table I.

TABLE I: OPTIMIZED PARAMETER VALUES FOR THE DUAL-BAND MTPA

Variable	Parameter Description	Size (mm)
w	width of the base material	70
l	length of the base material	70
l_p	length of a trapezoidal patch	31
w_{p1}	upper width of a trapezoidal patch	38
w_{p2}	lower width of a trapezoidal patch	32.53
α	flare angle at the left-lower-edge patch	100°
s_1	horizontal strip length	9
s_2	vertical strip length	21
s_3	strip width	7
h_s	height of the strip above the lower edge of the patch	12
l_f	feeding the microstrip line length	17
w_f	feeding the microstrip line width	3
l_g	ground plane length	15.5
w_g	ground plane width	33.1
g_1	feed-to-ground gap	0.4
g_2	patch-to-ground gap	1.5
t	copper layer thickness	0.035
h	thickness of the base material	1.6

To provide a clearer interpretation of the dual-band resonant behavior of the proposed antenna, an equivalent circuit representation is introduced, as depicted in Fig. 1(b) [27−29]. The developed model provides physical insight into the impedance-matching characteristics and the formation of resonances in the antenna structure. In this equivalent network, the Shape Memory Alloy (SMA) connector is represented by a series Resistor-Inductor-Capacitor (RLC) branch, whereas the CPW feed structure is modeled using two lumped transmission-line elements. In addition, three parallel RLC resonators are employed to emulate the electromagnetic responses of the main radiating patch, the modified flare-angle section, and the ILSS structure. A series resistance element is further incorporated to account for conductor and radiation losses. The initial circuit parameters are estimated using the formulation reported in the literature, followed by parameter optimization in the Advanced Design System (ADS) to achieve close agreement between the simulated and equivalent-circuit responses [27, 28].

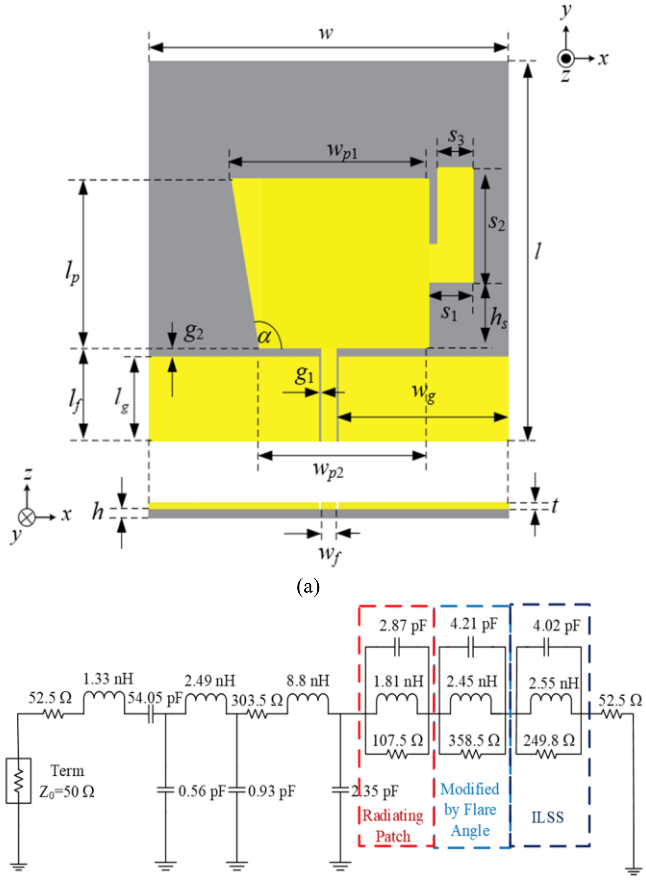

(a)

(b)

Fig. 1. Proposed antenna: (a) layout of the MTPA, (b) its equivalent circuit.

B. Stages of Antenna Design

The dual-band Modified Trapezoidal Patch Antenna (MTPA) was developed through a three-stage design process, as illustrated in Fig. 2. The first stage, Antenna #1 (Fig. 2(a)), consisted of a rectangular patch (38 mm × 31 mm) on a 1.6 mm-thick FR4 substrate (70 mm × 70 mm). A 50-Ω CPW feed, designed for resonance at 2.45 GHz, was used [30]. The feed line width (w_f) of 3 mm and length (l_f) of 17 mm were calculated for 50-Ω impedance (using Eqs. (3)−(5) from [31]). A 0.4 mm gap (g_1) was introduced between the feed line and the ground plane for impedance matching, as determined using the methods described in Refs. [31, 32]. The ground plane length l_g extended 15.5 mm beyond the bottom edge of the Radiating Rectangular Patch (RRP), with a 1.5 mm separation (g_2) between the RRP and the ground plane. Antenna #2 (Fig. 2(b)) was derived from Antenna #1 by cutting the lower-left edge at a flare angle (α) while maintaining the same width (w_{p1}). The final step involved attaching an ILSS to the right side of Antenna #2. The ILSS strip, with total length s_1+s_2, is designed to be approximately a quarter-wavelength at 2.45 GHz, thereby enhancing impedance matching and antenna gain. This results in the MTPA shown in Fig. 2(c).

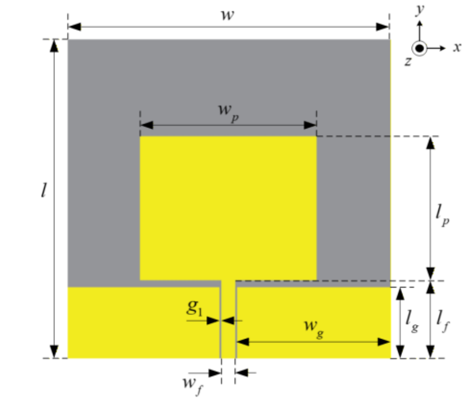

(a)

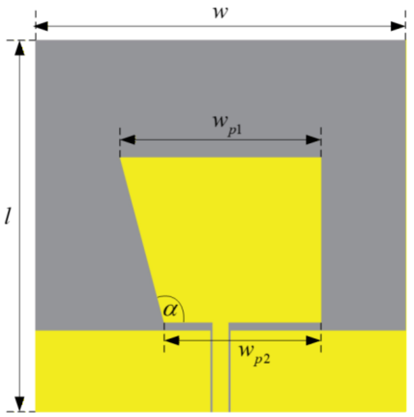

(b)

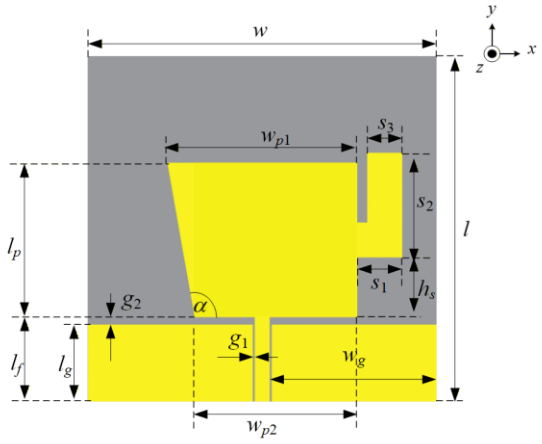

(c)

Fig. 2. The developed antenna: (a) Ant #1, (b) Ant #2, (c) proposed MTPA.

The design progression involved three distinct proto-types, each optimized to achieve specific performance goals. Antenna #1 served as the baseline design. It produced an omnidirectional radiation pattern with peak gains of 2.25 dBi at 2.45 GHz and 4.11 dBi at 7.5 GHz. This initial design demonstrated acceptable but limited bandwidths of 2.05 GHz to 3.38 GHz and 6.61 GHz to 8.43 GHz. The performance characteristics of Antenna #1 are visually represented in Fig. 3(a) and Fig. 4.

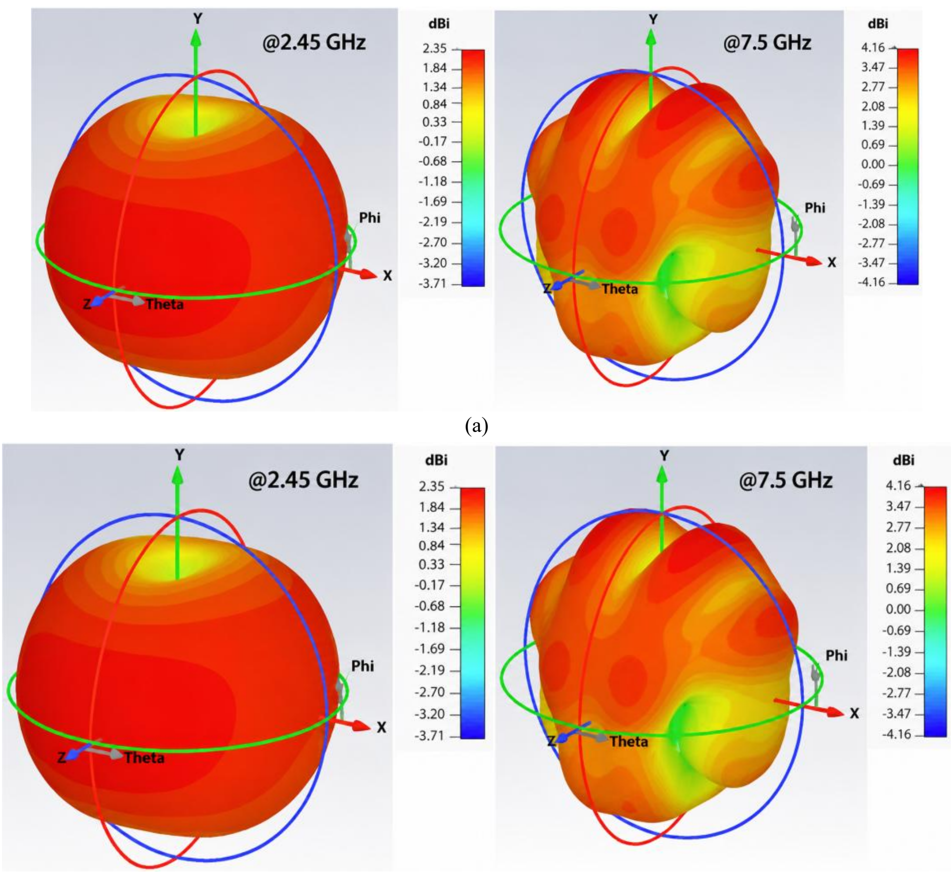

(a)

(b)

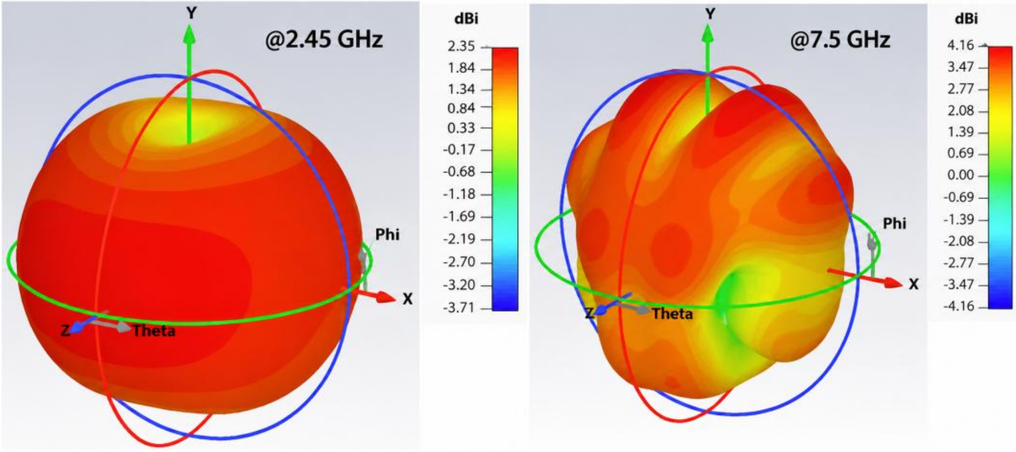

(c)

Fig. 3. 3D radiation pattern of (a) Ant#1, (b) Ant#2, and (c) proposed MTPA.

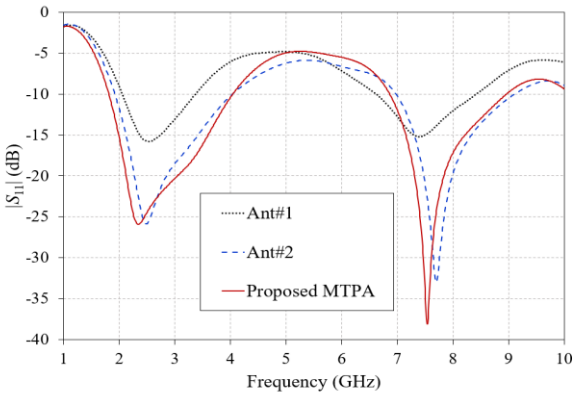

Fig. 4. Comparing the simulated $|S_{11}|$ of the developed antenna.

Antenna #2 introduced a significant modification that maintained the omnidirectional pattern while substantially improving the impedance matching and bandwidth. The peak gains dropped slightly to 2.09 dBi at 2.45 GHz and increased to 5.2 dBi at 7.5 GHz. More importantly, the 10 dB return loss bandwidth expanded dramatically from 1.92 GHz to 4.04 GHz and from 6.97 GHz to 9.12 GHz, as shown in Fig. 3(b) and Fig. 4. The flare-angle truncation at the lower-left edge alters the effective current path and reduces impedance discontinuities, thereby enhancing impedance matching and extending the bandwidth.

The final antenna combines the best attributes of the previous prototypes. It successfully maintains an omnidirectional radiation pattern while achieving two broad bandwidths: 1.81 GHz to 4.05 GHz and 6.86 GHz to 8.97 GHz. This final iteration delivers competitive gains of 2.65 dBi at 2.45 GHz and 3.93 dBi at 7.5 GHz. The detailed results for this optimized design are presented in Fig. 3(c) and Fig. 4. This progression from Antenna #1 to the final design demonstrates a methodical approach to optimizing both bandwidth and gain while preserving the essential omnidirectional pattern. The dual-band operation is attributed to the excitation of two resonant modes, where the modified trapezoidal patch primarily governs the lower-band resonance, while the ILSS introduces an additional resonant path for upper-band operation.

During the design process, the influence of key geometric parameters on achieving a 10 dB return loss was investigated. Fig. 5 illustrates the effect of the flare angle (α) on the reflection coefficient $|S_{11}|$. The results indicate that $|S_{11}|$ is highly sensitive to variations in α, primarily due to changes in the effective current path and impedance transition at the patch edge. A return loss of $|S_{11}| \leq -10$ dB is considered acceptable for good impedance matching, indicating efficient power transfer. The bandwidth enhancement can be attributed to the gradual increase in effective current path length and improved impedance transition at the patch edge as α increases. Among the tested configurations, $\alpha = 100°$ provided the best overall performance, maintaining $|S_{11}|$ below -10 dB across wide frequency bands of approximately 2 GHz to 4 GHz and 7 GHz to 9 GHz. Although wider angles (>100°) extended the bandwidth up to 9 GHz, they degraded $|S_{11}|$ performance at higher frequencies. In contrast, smaller angles ($\alpha < 90°$), where $w_{p_2} = w_p$ and w_{p_1} decreases, yielded only marginal improvement, with return loss remaining above the acceptable level. Conversely, larger angles ($\alpha > 105°$) induced frequency shifts and degraded upper-band matching. Therefore, $\alpha = 100°$ is identified as the optimal flare angle for achieving stable multiband impedance matching.

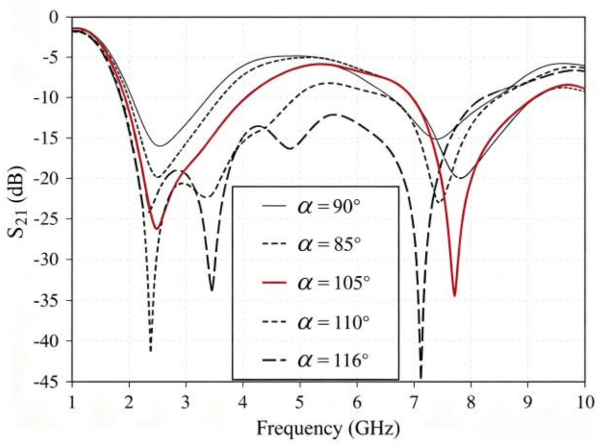

Fig. 5. $|S_{11}|$ as a function of α .

The influence of the ILSS (length s_1 and height h_s) on $|S_{11}|$ was then evaluated in Fig. 6 and Fig. 7. Various s_1 values (7 mm to 12 mm) were tested, with corresponding changes in length s_2 (21 mm to 18 mm) to keep the total length equal to 30 mm (about a quarter wavelength at 2.45 GHz), while maintaining s_3 at 7 mm and h_s at 12 mm. Fig. 6 shows that decreasing s_1 widened the bandwidth but degraded the lower-band $|S_{11}|$ performance, while the higher-band response was unchanged. An s_1 length of 12 mm yielded the best (deepest) dual-band $|S_{11}|$ response, yet offered the narrowest operating frequency range compared to 7 mm and 9 mm. Consequently, s_1 = 9 mm and s_2 = 21 mm were selected for the subsequent analysis, which assessed the effect of varying s_1 on $|S_{11}|$, as shown in Fig. 6.

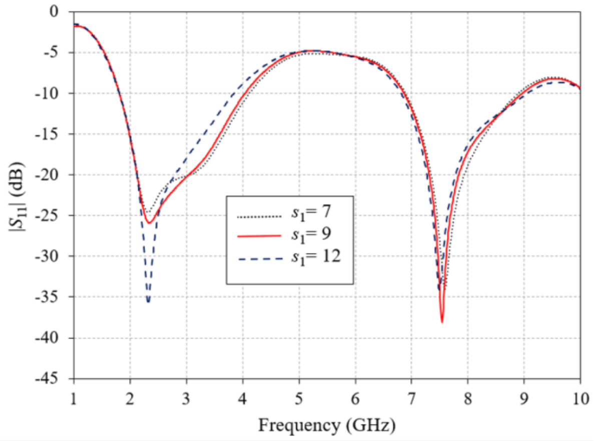

Fig. 6. $|S_{11}|$ as a function of s_1.

Then, the height h_s is varied while s_1, s_2, and s_3 are fixed as 9, 21, and 7 mm, respectively. In Fig. 7, the influence of the ILSS height position (h_s) on the antenna's resonant behavior and impedance performance was examined across five height levels (h_s = 0, 3, 12, 17, and 24 mm), starting from the configuration in which the bottom edge of the patch is aligned with the substrate surface (h_s = 0). At h_s = 0 mm, the antenna exhibited a resonance at 3.8 GHz with the lowest $|S_{11}|$ and the widest fractional 10 dB return loss bandwidth in the lower band. In contrast, the upper-band resonance at 8.12 GHz showed notably poor impedance matching. As h_s increased, the resonant frequencies of both operating bands generally shifted downward, indicating a strong sensitivity of the effective electrical length to vertical ILSS placement. An exception was observed for h_s = 17 and 24 mm, where the upper-band resonance shifted upward toward higher frequencies, suggesting a change in the current distribution and coupling mechanism at larger separations. Within the investigated range, h_s = 12 mm provided the most favorable impedance matching while accurately aligning the resonances with the desired dual-band targets (2.4 GHz to 2.5 GHz and 7.1 GHz to 8.4 GHz). Accordingly, h_s = 12 mm was selected as the optimal ILSS height position to achieve robust dual-band performance with enhanced matching characteristics.

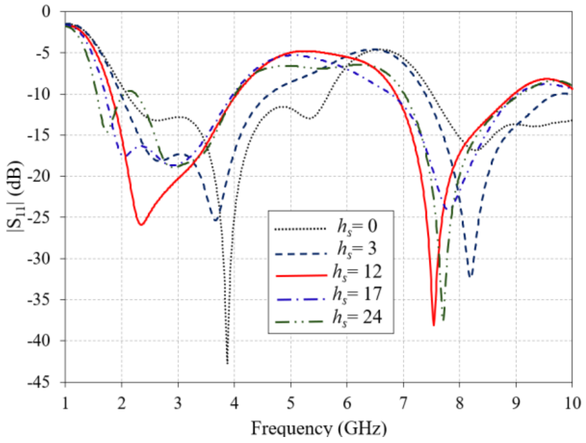

Fig. 7. $|S_{11}|$ as a function of h_s.

The proposed design achieves 10 dB return loss bandwidths of 1.81 GHz to 4.05 GHz (lower band) and 6.87 GHz to 8.97 GHz (upper band). In addition, gain was then examined as shown in Fig. 8. The final design exhibits an omnidirectional radiation pattern with gains ranging from 1.81 dBi to 4.94 dBi for the lower band, and 2.67 dBi to 4.1 dBi for the upper band. The corresponding radiation efficiencies ranged from 82.12% to 94.29% for the lower band, and 65.24% to 71.16% for the upper band.

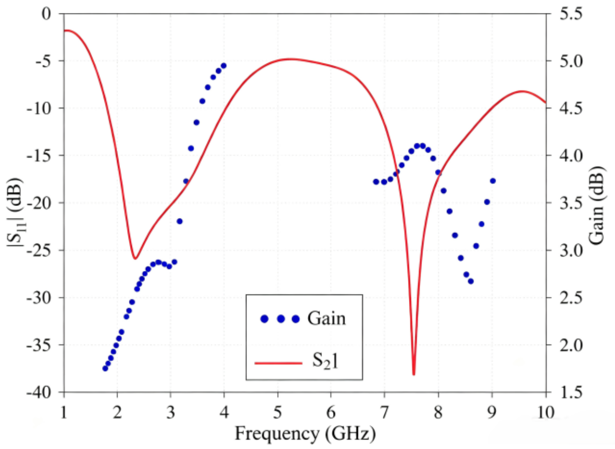

Fig. 8. Simulation results: $|S_{11}|$ and gain.

III. Experimental Results and Their Implications

To validate the numerical results, the prototype is fabricated on an FR4 substrate (relative permittivity of 4.3) with dimensions specified in Table I. Fig. 9(a) shows the top view of the fabricated prototype. The antenna is fed using a 50-Ohm SMA connector. The measurement setup used for validating the proposed antenna is illustrated in Fig. 9(b). The reflection coefficient $|S_{11}|$, radiation characteristics, and antenna gain were experimentally evaluated using a Keysight E5063A Vector Network Analyzer (VNA). Radiation pattern measurements were carried out inside a microwave anechoic chamber to minimize unwanted reflections and external electromagnetic interference. During the measurement process, two identical MTPA prototypes were employed in a transmitter–receiver configuration, where the Antenna Under Test (AUT) was mounted on a rotating platform with an angular step resolution of 1°. Furthermore, a separation distance of 60 cm between the transmitting and receiving antennas was maintained to satisfy the far-field measurement condition and ensure accurate characterization results.

(a)

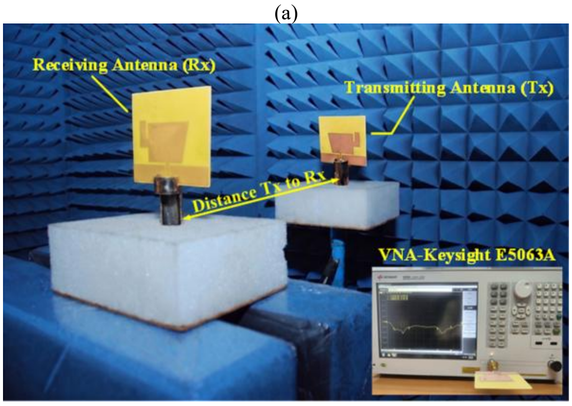

(b)

Fig. 9. The MTPA prototype: (a) top view, (b) measurement $|S_{11}|$ and radiation pattern setup.

Fig. 10 compares simulated and measured $|S_{11}|$. All data sets exhibit a similar trend, with minimal discrepancies likely attributed to minor differences between the simulation and measurement setups, such as the solder joint at the 50–Ohm SMA connector. The −10 dB bandwidths for WLAN and X-band applications were–CST simulation: 1.81 GHz to 4.05 GHz (76.5%), 6.87 GHz to 8.97 GHz (26.5%), ADS simulation: 1.75 GHz to 3.95 GHz (77.2%), 6.85 GHz to 9.2 GHz (29.3%), and measurement: 1.85 GHz to 3.57 GHz (63.5%), 7.12 GHz to 8.97 GHz (23%).

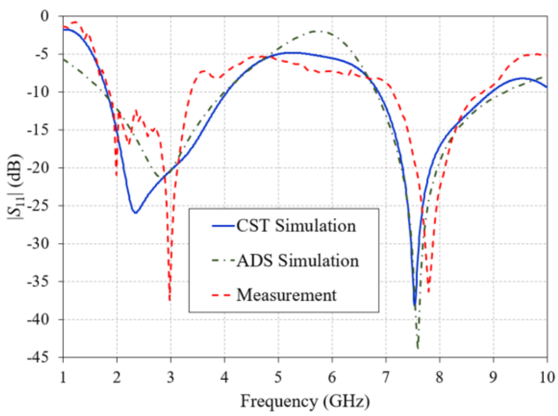

Fig. 10. Validation of MTPA performance: simulated vs. measured $|S_{11}|$.

To further validate the operating mechanism of the proposed antenna, the surface current distributions are examined. The surface current distributions at 2.45 GHz and 7.825 GHz are illustrated in Fig. 11. At 2.45 GHz, the current is primarily concentrated along the feed line and the lower region of the modified trapezoidal patch, forming a dominant current path corresponding to the fundamental resonant mode. The current distribution is relatively uniform across the patch, indicating that the radiation is mainly governed by the effective electrical length of the trapezoidal radiator. In contrast, at 7.825 GHz, the current distribution becomes more localized and intense along the ILSS and the adjacent edge of the patch. This behavior indicates that the ILSS introduces an additional resonant path, which contributes to the excitation of a higher-order mode. The interaction between the ILSS and the main patch leads to strong electromagnetic coupling, thereby generating the upper-band resonance and enhancing impedance matching in the X-band region. This observation confirms that the dual-band operation originates from two distinct current paths: the fundamental patch resonance at the lower band and the ILSS-assisted coupled resonance at the upper band.

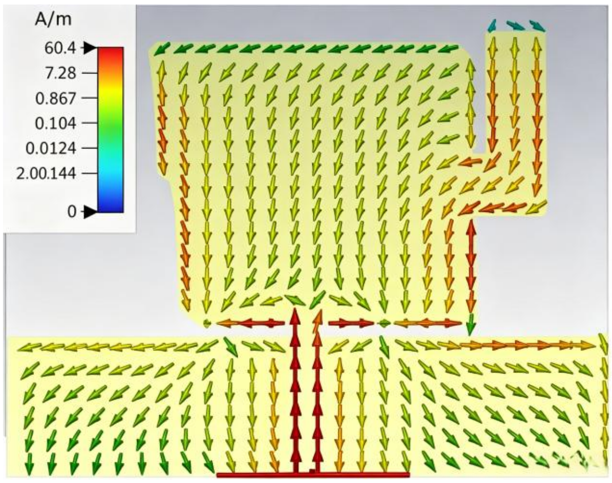

(a)

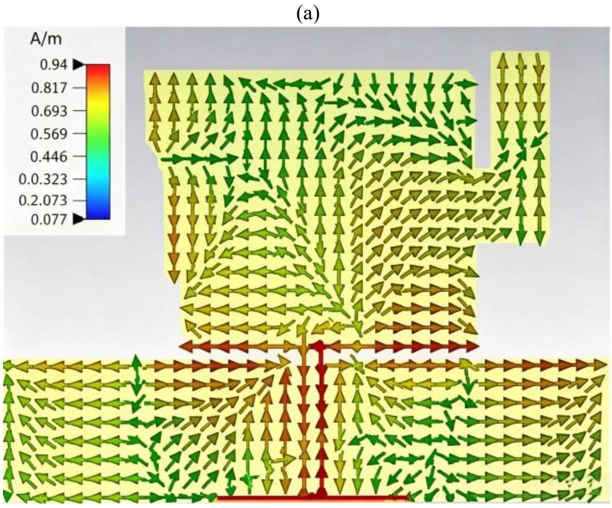

(b)

Fig. 11. Current distribution at (a) 2.45 GHz and (b) 7.825 GHz.

The radiation characteristics of the proposed dual-band patch antenna were evaluated at 2.45 GHz and 7.825 GHz in the *xz*-plane and *yz*-planes using identical antennas for transmission and reception, as illustrated in Fig. 12 and Fig. 13. Overall, the measured radiation patterns exhibit good agreement with minor discrepancies from the simulated results.

At 2.45 GHz, the antenna demonstrates a nearly omnidirectional pattern as expressed in 3D plotting in Fig. 12(a), and a 2D radiation pattern in the *xz*-plane (Fig. 12(b)) and a characteristic figure-eight pattern in the *yz*-plane (Fig. 12(c)), which is consistent with the expected behaviour of low-band omnidirectional operation.

At 7.825 GHz, slight pattern splitting is observed as exhibited in the 3D plot in Fig. 13(a); however, the 2D patterns in both planes maintain a general broad omnidirectional shape in the *xz*-plane (as seen in Fig. 13(b)) and a figure-eight response in the *yz*-plane as plotted in Fig. 13(c), similar to the low-frequency behaviour. The slight pattern distortion observed at the upper band is likely due to higher-order mode excitation and increased surface current concentration along the ILSS region.

This antenna exhibits linear polarization with cross-polarization levels below –20 dB across both operating bands, confirming stable polarization purity. he simulated peak gains of 2.65 dBi at 2.45 GHz and 4.06 dBi at 7.825 GHz correspond closely to the measured peak gains of 2.71 dBi and 3.69 dBi, respectively, as shown in Fig. 14. Furthermore, the minimum and maximum simulated gains are 2.59/2.87 dBi for the 2.4 GHz WLAN band and 2.93/4.10 dBi for the upper-band Fixed-Satellite Service (FSS) region. These values agree well with the minimum/maximum measured gains of 2.58/2.72 dBi and 2.74/3.84 dBi for the lower and upper bands, respectively. Additionally, the radiation efficiencies range from 82.12% to 94.35% in the lower band and 65.23% to 71.13% in the upper band, demonstrating that the antenna maintains high efficiency across the targeted operational frequencies.

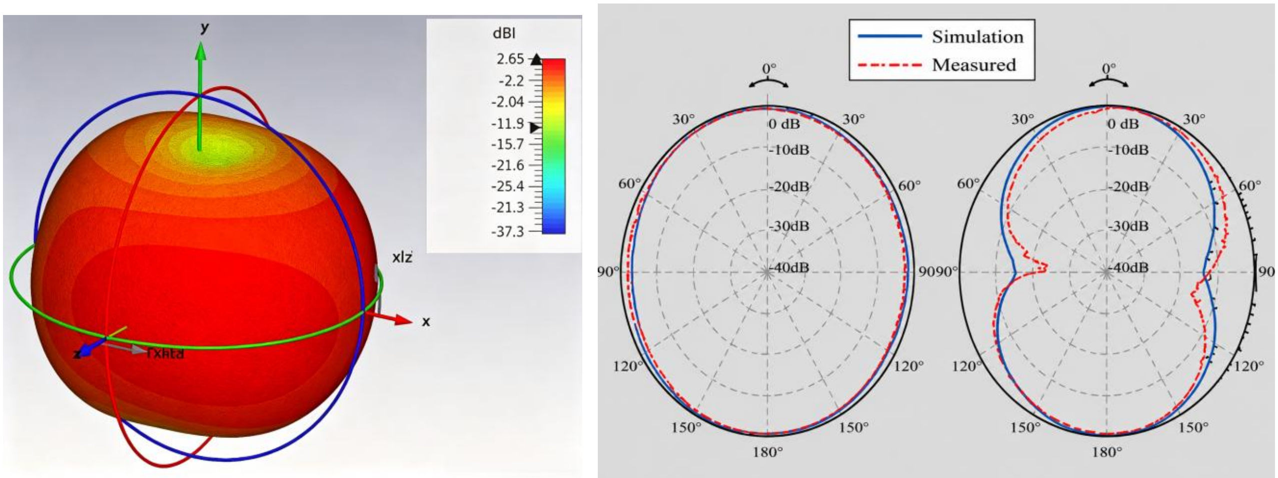

(a) (b) (c)

Fig. 12. Simulated and measured radiation patterns at 2.45 GHz: (a) 3D, (b) *xz*-plane, (c) *yz*-plane.

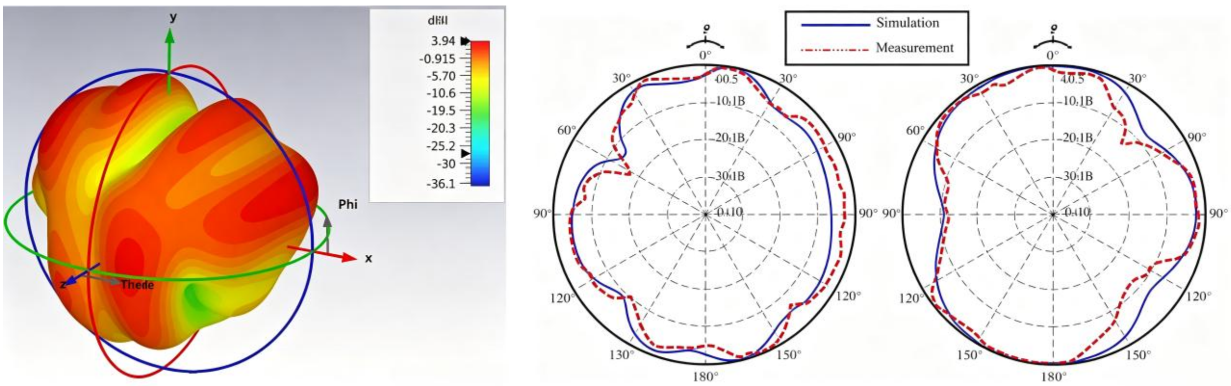

(a) (b) (c)

Fig. 13. Simulated and measured radiation patterns at 7.825 GHz: (a) 3D, (b) *xz*-plane, (c) *yz*-plane.

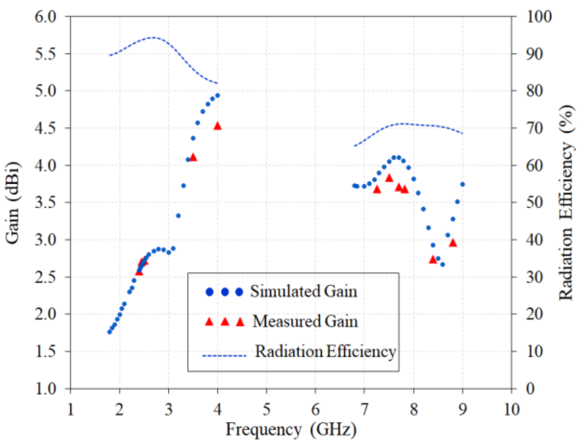

Fig. 14. Simulated and measured gain and radiation efficiency.

Table II provides a comprehensive comparative analysis between the proposed antenna and state-of-the-art dual-band designs, evaluated based on normalized electrical dimensions, impedance bandwidth, radiation characteristics, and structural topology. To ensure an equitable comparison, all physical dimensions are normalized to the free-space wavelength at the lower operating frequency (λ_L). A critical review of the literature reveals a persistent trade-off between bandwidth enhancement and profile height. For instance, while the metallic-wire discone [8] and orthogonal balun-based [21] configurations achieve broad bandwidths and high gains, their high-profile architectures and increased structural complexity significantly impede their integration into compact, low-profile wireless terminals. In the domain of planar designs, antennas utilizing parasitic patches [9, 17] or modified circular geometries [16] offer improved compactness. However, the comparative design occupies a larger area of (0.50 λ_L × 0.50 λ_L) [16]. Despite having a similar physical size, the proposed antenna delivers superior upper-frequency coverage from 7.12 GHz to 8.97 GHz relative to the 4.59–8.16 GHz range of the reference structure [17]. Furthermore, although transparent [10] and wearable [18] alternatives offer mechanical versatility, they face significant performance limitations. Specifically, the transparent antenna in Ref. [10] suffers from a drastic reduction in realized gain (from –0.145 to –3.9 dBi) and radiation efficiency (10% to 15%) due to the high ohmic losses of the ITO material. Similarly, the loop-based design in Ref. [11] lacks comprehensive gain reporting and relies on a –6 dB impedance bandwidth criterion, which may not meet the stringent requirements of modern communication standards. In contrast, the proposed patch-with-stub antenna provides a favorable trade-off between size, simplicity, and upper-band performance. With a footprint of 0.43λ_L × 0.43λ_L × 0.01λ_L, it yields a dual-band response spanning 1.86 GHz to 3.57 GHz and 7.12 GHz to 8.97 GHz. Despite its simple planar structure, the antenna maintains omnidirectional radiation with peak gains of 2.72 dBi and 3.84 dBi. These attributes, combined with competitive efficiency and ease of fabrication on a standard FR4 substrate, validate the proposed design as a robust candidate for integrated WLAN and X-band applications. Therefore, the proposed antenna achieves a balanced trade-off among structural simplicity, dual-band operation, and radiation performance, making it more suitable for practical planar wireless systems than many existing designs.

TABLE II: COMPARATIVE PERFORMANCE EVALUATION OF THE PROPOSED DUAL-BAND ANTENNA AGAINST STATE-OF-THE-ART

Ref.	Antenna type	Material	Dimension (λ_L)	Bandwidth (–10 dB)	Pattern	Structure complexity	Gain (dBi)	Eff. (%)
[8]	Metallic wire-discone, printed meanderline, and stubs	Metallic & RT 5870	0.3 × 0.3 × 0.048 (100 × 100 × 16 mm^3)	0.9 GHz, 2–6 GHz (sim)	omnidirectional	medium	7 (sim)	95
[9]	Ring + vias + embedded parasitic patch	FR4	π (0.515)^2 × 0.055 (π (90)^2 × 9.6 mm^3)	1.71–2.28 GHz, 2.41–2.57 GHz	omnidirectional	less	4.462	85
[10]	Transparent antenna	ITO/Glass	0.30 × 0.10 × 0.01 (50 × 17 × 1.1 mm^3)	1.82–2.5 GHz, 4.66–11.84 GHz	omnidirectional	less	–0.145 –3.9	10–15
[11]	Loops	FR4	0.29 × 0.59 × 0.01 (40 × 80 ×1.4 mm^3)	2.20–2.65 GHz, 4.81–7.45 GHz (–6dB)	omnidirectional	medium	n/a	60.7–53.4
[16]	Modified circular patch antenna	FR4	0.50 × 0.50 × 0.01 (62 × 62 × 1.6 mm^3)	2.4–3 GHz, 5.6–6.4 GHz	omnidirectional	less	1.8–3.25	85–90
[17]	Patch with parasitic	FR4	0.40 × 0.40 × 0.01 (70 × 70 × 1.6 mm^3)	1.7–3.44 GHz, 4.59–8.16 GHz	omnidirectional	less	2.92–4.25	<86.92 <77.64
[18]	Wearable antenna	RT5880	0.26 × 0.14 × 0.004 (32 × 17 × 0.5 mm^3)	2.3–2.55 GHz, 5.42–6 GHz	omnidirectional	less	1.32–4.76	97.9–91.4
[21]	Orthogonal balun pairs, resonant ring, four angular columns, and radiating surface	Metal & FR4	0.8 × 0.8 × 0.18 (140 × 140 × 30 mm^3)	1.71–2.17 GHz, 3.22–3.7 GHz	unidirectional	more	7–7	80–80
This work	Patch with stub	FR4	0.43 × 0.43 × 0.01 (70 × 70 ×1.6 mm^3)	1.86–3.57 GHz, 7.12–8.97 GHz	omnidirectional	less	2.72 3.84	<82.12 <65.23

Note: λ_L is the free-space wavelength at the lower operating frequency. Sim: Simulated.

IV. Conclusion

This paper presents a modified trapezoidal-shaped antenna for dual-band operation, covering the 2.4–2.5 GHz WLAN band and the X-band (7.1–7.75 GHz downlink/7.9–8.4 GHz uplink). The antenna is fabricated on a single-layer FR4 substrate and utilizes a 50-Ω coplanar waveguide feed. The design incorporates a flare-angle truncation at the lower-left edge of the patch to improve impedance matching, along with an inverted L-shaped strip to enhance both impedance matching and radiation performance. Measured results are in good agreement with simulations, demonstrating peak gains of 2.72 dBi at 2.5 GHz (WLAN) and 3.84 dBi at 7.5 GHz (FSS) under linear polarization. The antenna exhibits a simple planar structure with stable omnidirectional radiation patterns, making it suitable for both indoor and outdoor WLAN and X-band applications. The proposed design provides a practical solution for dual-band wireless systems, with potential applicability in satellite and emerging high-frequency communication platforms. Future work will focus on integrating Machine Learning (ML) techniques for automated antenna geometry optimization and adaptive frequency tuning. In addition, the extension to MIMO configurations and array-based implementations for high-gain applications will be investigated.

Conflict of Interest

The authors declare no conflict of interest.

Author Contributions

Suthasinee Lamultree conceived the conceptualization and methodology, while Punyawat Wiyanat and Kanit Butdaengnoi conducted and collected the data. Suthasinee Lamultree investigated, analyzed, and wrote the paper; Chuwong Phongcharoenpanich is the supervisor of the research; all authors have approved the final version.

Funding

This research project is supported by Science Research and Innovation Fund Agreement No. FF69/KKC/037, Rajamangala University of Technology Isan, Khonkaen Campus.

References

[1] K. Srivastava, A. Kumarb, B. K. Kanaujia *et al.*, "Multiband integrated wideband antenna for bluetooth/WLAN applications," *AEU-International Journal of Electronics and Communications*, vol. 89, pp. 77–84, 2018.

[2] Y. Jay Guo, C. A. Guo, M. Li, and M. Latva-aho, "Antenna technologies for 6G–Advances and challenges," *IEEE Trans. on Antennas and Propagation*, vol. 74, no. 5, pp. 3865–3880, 2025.

[3] M. A. Al-Mihrab, A. J. Salim, and J. K. Ali, "A compact multiband printed monopole antenna with hybrid polarization radiation for GPS, LTE, and satellite applications," *IEEE Access*, vol. 8, pp. 110371–110380, 2020.

[4] T. Saeidi, I. Ismail, S. Noghanian *et al.*, "High gain triple-band metamaterial-based antipodal vivaldi MIMO antenna for 5G communications," *Micromachine*s, vol. 12, no. 3, 250, pp. 1–24, 2021.

[5] H. C. Ye, C. Mao, L. L. Dai, and X. Y. Zhang, "Dual-band dual-polarized antenna and array with enhanced bandwidth for 5G millimeter-wave applications," *IEEE Antennas Wirel. Propag. Lett.*, vol. 24, no. 7, pp. 1829–1833, July 2025.

[6] S. V. Yadav *et al.*, "Multi-band high-frequency antenna for satellite, automotive radar, and 6G communication," *Sci. Rep.*, vol. 15, 30400. 2025.

[7] A. M. Ahmed, S. A. Majeed, Y. S. Dawood, "A survey of 6G mobile systems, enabling technologies, and challenges," *International Journal of Electrical and Electronic Engineering and Telecommunications*, vol. 12, no. 1, pp. 1–12, 2023.

[8] M. J. Saeed, M. M. Tahseen, and A. A. Kishk, "Compact multiband omnidirectional antenna for maximizing frequency coverage," *IEEE Antennas Wirel. Propag. Lett.*, vol. 24, no. 3, pp. 597–601, 2025.

[9] E. T. Ashong, S. Bang, J. Y. Chung, "Dual-band multilayer patch antenna for multiband internet-of-vehicles applications," *Electronics*, vol. 14, no. 22, 4400, 2025.

[10] J. I. T. Flores *et al.*, "CPW-fed transparent antenna for vehicle communications," *Appl. Sci.*, vol. 10, no. 17, 6001, 2020.

[11] R. Li *et al.*, "Miniaturized antenna design for dual-band Wi-Fi 6/6E applications using the ground radiation technique," *JEES*, vol. 25, no. 2, pp. 202–204, 2025.

[12] M. Z. Chowdhury *et al.*, "6G wireless communication systems: applications, requirements, technologies, challenges, and research directions," *IEEE Open J. Commun. Soc.*, vol. 1, pp. 957–975, 2020.

[13] G. Rajesh and R. Poonkuzhali, "Design and analysis of CPW fed ultrathin flexible MIMO antenna for UWB and X-band applications," *IEEE Access*, vol. 12, pp. 96704–96717, 2024.

[14] A. Chaabane *et al.*, "Multiband stepped antenna for wireless communication applications," *Informacije Midem*, vol. 50, no. 4, pp. 275–283, 2020.

[15] S. U. Rahma and Q. Cao, "Compact design of trapezoid shape monopole antenna for SWB application," *Microw. Opt. Technol. Lett.*, vol. 61, no. 8, pp. 1931–1937, 2019.

[16] E. D. K. Ruby *et al*, "Compact circularly polarized dual band antenna with modified patch for ISM and V2X communication systems," *Sci. Rep.*, vol. 15, no. 1, 5885, 2025.

[17] S. Lamultree, S. Ungprasutr, C. Saetiaw, and C. Phongcharoenpanich, "A dual-band modified-rectangular patch with parasitic antenna for 2.4/5 GHz wireless local area network applications," *Telkomnika*, vol. 23, no. 5, pp. 1177–1187, 2025.

[18] G. K. Soni *et al.*, "Design of a compact multistubs resonator based dual-band flexible wearable antenna with low SAR for sub-6 GHz ISM applications," *Sci. Rep.*, vol. 15, 24013, 2025.

[19] A. A. Nikam and R. B. Patil, "Design and development of multiband PIFA antenna for vehicular LTE/5G and V2X communication," *J. Wireless. Com. Network*, vol. 2023, no. 1, pp. 1–15, 2023.

[20] A. Annou, S. Berhab, and F. Chebbara, "Metamaterial-fractal-defected ground structure concepts combining for highly miniaturized triple-band antenna design," *Journal of Microwaves Optoelectronics and Electromagnetic Applications*, vol. 19, no. 4, pp. 522–541, 2020.

[21] J. Li, J. Li, J. Yin, C. Guo, H. Zhai, and Z. Zhao, "A miniaturized dual-band dual-polarized base station antenna loaded with duplex baluns," *IEEE Antennas Wirel. Propag. Lett.*, vol. 22, no. 7, pp. 1756–1760, July 2023.

[22] A. Kumar, G. Singh, M. K. Abdulhameed, S. R. Hashim, and A. J. A. A. Gburi, "Development of fractal 5G MIMO antenna for sub 6 GHz wireless automotive applications," *Progress in Electromagnetics Research M*, vol. 130, pp. 121–128, 2024.

[23] M. E. Hammoumi *et al.*, "A wideband circularly polarized CPW-fed printed monopole X-Band Antenna for cubesat applications," *IEEE Access*, vol. 11, pp. 121077–121086, 2023.

[24] B. Y. Akowuah *et al.*, "Study of a printed split-ring monopole for dual-spectrum communications," *Heliyon*, vol. 7, no. 9, e0792, 2021.

[25] N. Hussain *et al.*, "A compact tri-band antenna based on inverted-L stubs for smart devices," *Computers, Materials & Continua*, vol. 7, no. 2, pp. 3321–3330, 2022.

[26] Computer Simulation Technology. Microwave Studio. Research Base. (2016). [Online]. Available: https://sigmasolutions.co.th/en/cst-studio-suite
[27] A. A. Abdulbari *et al*., "Single-layer planar monopole antenna-based Artificial Magnetic Conductor (AMC)," *International Journal of Antennas and Propagation*, vol. 2022, no. 1, pp. 1–9, 2022.
[28] M. Y. Zeain *et al*., "A new technique of FSS-based novel chair-shaped compact MIMO antenna to enhance the gain for sub-6GHz 5G applications," *IEEE Access*, vol. 12, pp. 49489–49507, 2024.
[29] B. Luadang *et al*., "Broadband unidirectional twin-element MIMO antenna scheme for mid-band 5G and WLAN laptops," *Sci. Rep.* vol. 14, no. 1, 9693, 2024.
[30] C. A. Balanis, *Antenna Theory: Analysis and Design*, John Wiley and Sons, 2012.
[31] S. Lamultree, S. Srisukhot, C. Saetiaw, K. Nuangwongsa, C. Phongcharoenpanich, "Design of a compact wideband bi-directional pattern antenna for 5G applications," *Eureka: Physics and Engineering*, no. 4, pp. 40–51, 2023.
[32] R. E. Collin, *Foundations for Microwave Engineering*, John Wiley and Sons, 2007.

Suthasinee Lamultree received the B. Eng. and M. Eng. in telecommunication engineering from King Mongkut's Institute of Technology Ladkrabang, Thailand, in 2000 and 2003, respectively. In 2009, she received her D.Eng. in electrical engineering from the same institution. In 2016, she joined the Department of Electronics and Telecommunication Engineering, Faculty of Engineering, Rajamangala University of Technology Isan Khonkaen Campus, Khonkaen, Thailand. Her research interests include antenna design, microwave technology, and wireless communication systems.

Punyawat Wiyanat received the B.Eng. in electronics and telecommunication engineering from the Faculty of Engineering, Rajamangala University of Technology Isan Khonkaen Campus, Thailand, in 2023. His research interests include antenna and circuit design.

Kanit Butdaengnoi received the B.Eng. in electronics and telecommunication engineering from the Faculty of Engineering, Rajamangala University of Technology Isan Khonkaen Campus, Thailand, in 2023. His research interests include antenna and circuit design.

Chuwong Phongcharoenpanich was awarded his honors bachelor of engineering, master of engineering and doctor of engineering degrees from King Mongkut's Institute of Technology Ladkrabang (KMITL), Bangkok, Thailand, in 1996, 1998 and 2001 respectively. He currently holds the rank of professor within the Department of Telecommunications Engineering at KMITL, and additionally acts as the director of the Innovative Antenna and Electromagnetic Applications Research Laboratory. His research activities center on antenna design suited for diverse mobile and wireless communication hardware, conformal antenna technology, as well as the theory of antenna arrays.